PAPER • OPEN ACCESS

Influence of the magnetic field on the discharge physics of a high power impulse magnetron sputtering discharge

To cite this article: M Rudolph *et al* 2022 *J. Phys. D: Appl. Phys.* **55** 015202

View the article online for updates and enhancements.

Influence of the magnetic field on the discharge physics of a high power impulse magnetron sputtering discharge

M Rudolph[1,*] , **N Brenning**[2,3] , **H Hajihoseini**[4] , **M A Raadu**[3], **T M Minea**[5] , **A Anders**[1,6] , **J T Gudmundsson**[3,7] **and D Lundin**[2]

[1] Leibniz Institute of Surface Engineering (IOM), Permoserstraße 15, 04318 Leipzig, Germany
[2] Plasma and Coatings Physics Division, IFM-Materials Physics, Linköping University, SE-581 83 Linköping, Sweden
[3] Space and Plasma Physics, School of Electrical Engineering and Computer Science, KTH Royal Institute of Technology, SE-100 44 Stockholm, Sweden
[4] Industrial Focus Group XUV Optics, MESA+ Institute for Nanotechnology, University of Twente, Drienerlolaan 5, 7522 NB Enschede, The Netherlands
[5] Université Paris-Saclay, CNRS, Laboratoire de Physique des Gaz et des Plasmas, 91405 Orsay, France
[6] Felix Bloch Institute of Solid State Physics, Leipzig University, Linnéstraße 5, 04103 Leipzig, Germany
[7] Science Institute, University of Iceland, Dunhaga 3, IS-107 Reykjavik, Iceland

E-mail: martin.rudolph@iom-leipzig.de

CrossMark

Abstract

The magnetic field is a key feature that distinguishes magnetron sputtering from simple diode sputtering. It effectively increases the residence time of electrons close to the cathode surface and by that increases the energy efficiency of the discharge. This becomes apparent in high power impulse magnetron sputtering (HiPIMS) discharges, as small changes in the magnetic field can result in large variations in the discharge characteristics, notably the peak discharge current and/or the discharge voltage during a pulse. Here, we analyze the influence of the magnetic field on the electron density and temperature, how the discharge voltage is split between the cathode sheath and the ionization region, and the electron heating mechanism in a HiPIMS discharge. We relate the results to the energy efficiency of the discharge and discuss them in terms of the probability of target species ionization. The energy efficiency of the discharge is related to the fraction of pulse power absorbed by the electrons. Ohmic heating of electrons in the ionization region leads to higher energy efficiency than electron energization in the sheath. We find that the electron density and ionization probability of the sputtered species depend largely on the discharge current. The results suggest ways to adjust electron density and electron temperature using the discharge current and the magnetic field, respectively, and how they influence the ionization probability.

---

* Author to whom any correspondence should be addressed.

1

(Some figures may appear in colour only in the online journal)

1. Introduction

For over four decades the magnetron sputtering discharge has been applied successfully for deposition of thin films and coatings with applications in various fields in both academia and industry [1, 2]. The magnetron sputtering discharge is a magnetically enhanced glow discharge where the residence time of the electrons in the vicinity of the cathode target is extended by the presence of a static magnetic field. In the planar circular configuration, this is done by concentrically placing a central cylindrical magnet and an outer edge ring magnet behind the cathode target, with anti-parallel magnetization. In the presence of such a magnetic field, the discharge voltage is lowered, the working gas pressure can be decreased, and the deposition rate is substantially increased, compared to non-magnetized dc diode sputtering [3, 4]. In this planar circular magnetron configuration, the static magnetic field is arranged in such a way that the electrons drift azimuthally. The magnetic field strength is typically in the range 20–50 mTesla [3], so the electrons are magnetized, while the magnetic field does not influence the ion trajectories directly [5].

The magnetic field strength and the degree of magnetic unbalance have a significant influence on the discharge current and/or the discharge voltage. This is particularly true for the high power impulse magnetron sputtering (HiPIMS) discharge, in which small changes in the magnetic field strength and/or degree of unbalance can give strong variations of the discharge current waveform and the discharge voltage [6–8]. For a fixed discharge voltage, an increased magnetic field strength leads to an increased peak discharge current. For a fixed peak discharge current, increasing the magnetic field strength decreases the discharge voltage [8]. The degree of magnetic unbalance also influences both the discharge voltage and current, but these effects are less well studied.

The key to understanding the changes in the discharge voltage and current waveforms lies in how the discharge voltage V_D is split between the cathode sheath and the ionization region (IR). The presence of a transverse magnetic field enables a potential drop to exist outside the cathode sheath [9–12]. In sputtering magnetrons, this potential outside the sheath is denoted as V_{IR}, where the subscript IR signifies the ionization region in the vicinity of the cathode target. The discharge voltage thereby falls over the cathode sheath and the IR, i.e. $V_D = V_{SH} + V_{IR}$, where V_{SH} is the sheath potential drop. Unlike non-magnetized dc diode sputtering discharges, which are primarily maintained by ion-induced emission of secondary electrons accelerated in the cathode sheath [1, 13], the addition of a potential V_{IR} across the IR enables Ohmic heating of the electrons [14], which describes locally absorbed power by the electrons within the IR. In magnetron sputtering

discharges, this results in an energy gain by electrons that are moved across a fraction of the potential drop V_{IR}.

Ohmic heating is believed to be the dominating electron power absorption mechanism of HiPIMS discharges [15, 16]. More importantly, though, it is accompanied with less ion acceleration, compared to sheath energization. This is because the current in the IR is composed of both ions and electrons in equal shares, compared to the sheath, where the current is composed mostly of ions, while electrons make up only a few % due to an effective secondary electron emission yield of around 0.05 [16]. Therefore, the total power that is necessary to heat electrons by Ohmic heating is only 10%–20% compared to the power needed to heat electrons by the same amount in the sheath [16]. Total power here means the power dissipated by both electrons and ions. The result is that for discharges with a higher fraction of Ohmic heating over total electron heating (Ohmic heating plus sheath energization), the same discharge current can be maintained at a lower discharge voltage. The discharge becomes more energy-efficient.

There are indications that the ratio of Ohmic heating to sheath heating changes depending on the magnetic field configuration. Mishra *et al* [17] observed a decrease in V_{IR} with decreasing magnetic field strength by emissive probe measurements. Computational modeling of HiPIMS discharges show that a weaker magnetic field results in weaker Ohmic heating in combination with a decreasing voltage fraction across the ionization region, i.e. $f = V_{IR}/V_D$ decreases with decreasing magnetic field strength [16]. Despite these results, there is still a limited understanding of to what extent the magnetic field influences changes in Ohmic heating within the IR.

In the present work, therefore, we address the challenge on how the magnetic field affects internal discharge parameters, like the electron density and electron temperature, how it changes the relative contribution of each of the two electron power absorption mechanisms, Ohmic heating and sheath energization, and how these variations in the discharge properties in turn influence a key property of a HiPIMS discharge, the probability of target species ionization. This is done by modelling several HiPIMS discharges. The HiPIMS discharges are taken from the experimental studies of Hajihoseini *et al* [8] who studied magnetron sputtering discharges with varying magnetic field configurations. The modelling is done using an updated version of the ionization region model (IRM) [18, 19]. The IRM is a time-dependent volume-averaged plasma chemical model of the dense plasma in the ionization region adjacent to the cathode target racetrack [3, 4]. The experimental discharge current–voltage waveforms used to lock the IRM are here extended to include the ionized flux fraction [20] for each of the investigated discharges. Also, the IRM is improved by including consideration of an afterglow [18], and a revision of electron impact excitation and ionization cross sections [19].

These changes make it possible to better lock the IRM and thereby establish key trends in discharge parameters versus magnetic field configuration with smaller error bars on all calculated parameters.

In section 2, we shortly describe the setup of the experimental discharges and the modelling of these discharges using the IRM. Section 3 discusses the results and is split up into discussing the influence of the magnetic field configuration on the electron density (section 3.1), on the electron heating and the corresponding electron temperature (section 3.2), and the combined effect of density and electron temperature on the ionization probability of target species (section 3.3). A summary is provided in section 4.

2. Experimental and model description

The modelling done here is based on experimental discharges analyzed by Hajihoseini *et al* [8], in which the focus of the study was on how the magnetic field strength and degree of unbalance influence the deposition rate and the degree of ionization in the flux of film forming species towards the substrate. In the studied discharges the working gas pressure was kept constant at $p_{gas} = 1$ Pa, the pulse length at $t_{pulse} = 100$ μs, and the average discharge power at $\langle P_D \rangle = 300$ W, as the magnetic field strength and degree of unbalance were varied.

2.1. The electron-confining magnetic field of the magnetron assembly

The magnetron assembly used for the discharges in Hajihoseini *et al* [8] had an adjustable confining magnetic field. It was a planar circular magnetron assembly with a 4 inch target diameter and consisted of a center (C) and an annular edge (E) magnet pack. The distance of each magnet pack from the target rear could be adjusted. The magnetic field configurations obtained in this way were denoted Cz_CEz_E where z_C and z_E were distances in mm measured from the position closest to the rear of the target. The definition of z_C and z_E is shown schematically in figure 1. E.g. the magnetic configuration C0E5 meant that the central magnet was positioned closest to the rear of the target, while the annular edge magnet was 5 mm away from the position closest to the rear of the target [8]. The magnetic field configurations that could be obtained by the magnetron assembly described above, were all of unbalanced type II based on the definition of Window and Savvides [21].

The magnetic field configurations were characterized in Hajihoseini *et al* [8] by two magnetic field parameters determined from mapping the magnetic field $\mathbf{B}(z, r)$ above the target surface: (a) the magnetic field strength at 11 mm above the racetrack, B_{rt}, and (b) the distance to the magnetic null point measured from the target surface, z_{null}. The magnetic field parameters B_{rt} and z_{null} are defined in figure 1.

Instead of using the magnetic field parameters B_{rt} and z_{null}, we here use the sum of the two distances of the central and the edge magnet from the rear of the target to describe the magnetic field. We denote this constructed parameter $z_{gap} = z_C + z_E$. Table 1 gives the values of the three parameters
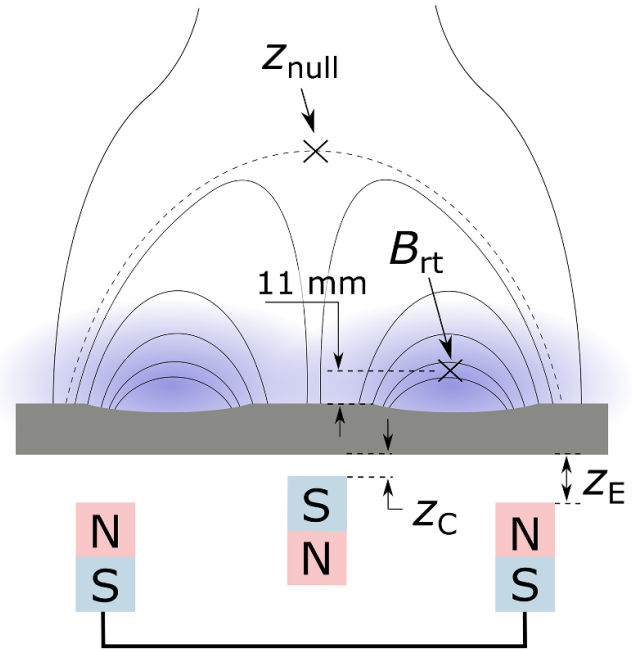

Figure 1. Schematic drawing of the magnetron assembly with definitions of the parameters B_{rt} and z_{null}, and the distance coordinates z_C and z_E for the central (C) and the annular edge (E) magnet with respect to their closest position to the rear of the target, respectively.

Table 1. The three magnetic field parameters z_{gap}, B_{rt}, and z_{null}, which can be used to describe a magnetic field configuration, for the seven different studied magnetic field configurations. The values for B_{rt} and z_{null} are taken from Hajihoseini *et al* [8].

Magnetic field configuration	z_{gap} (mm)	B_{rt} (mT)	z_{null} (mm)
C0E0	0	23.3	66
C0E5	5	21.7	70
C0E10	10	21.3	74
C5E0	5	18.1	53
C5E5	10	16.1	59
C10E0	10	13.7	43
C10E10	20	11.1	52

z_{gap}, B_{rt}, and z_{null} for the seven studied magnetic field configurations. The reason for using z_{gap} rather than the often used or 'classical' magnetic field parameters B_{rt} and z_{null}, is that this parameter captures rather well similarities between discharges having very different magnetic field configurations. As shown below, certain discharge parameters exhibit smooth trends with variations of z_{gap} and discharges with the same z_{gap} show similar values of these parameters. It is therefore an empirically verified similarity parameter. We also note that z_{gap} can remotely be related to the measured magnetic field parameters. It is intuitively clear, that by moving any of the two magnet packs away from the rear of the target, the contribution to the magnetic field above the target is reduced. Note that this is not a localized change of the magnetic field strength but it is rather an integral change of the magnetic field strength in the whole volume of the IR. Figure 2 shows the relation of z_{gap} to the measured parameter B_{rt}. The dashed line is a linear fit to the three configurations where both the magnet packs are
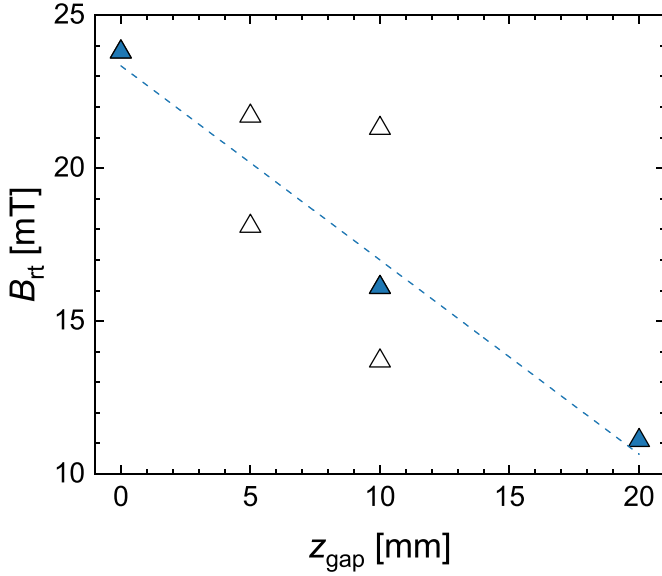
Figure 2. The magnetic field strength B_{rt}, measured 11 mm above the racetrack, versus z_{gap}. The dashed line is a linear fit through the three configurations where the magnetic packs are moved together, C0E0, C5E5, and C10E10 (filled blue triangles).

moved together (filled blue triangles). For these configurations there is an almost linear trend of decreasing B_{rt} for increasing z_{gap}. However, the other configurations, in which the two magnets are at different distances from the target, give a considerable scatter around this trend. Note, that the discussion here is based on the stationary magnetic field that is due to the permanent magnets (the magnet packs). It has been demonstrated through measurements that the magnetic field can be deformed by the azimuthal currents (Hall drift and diamagnetic drift) in the discharge, and changes of up to 1–2 mTesla have been reported [22]. The deformation depends on the spatial location and appears to be up to roughly 10% of the magnetic field just above the racetrack region.

The choice of magnetic configuration has a very large impact on the discharge properties. For example, between the two extreme configurations C0E0 to C10E10, the peak discharge current $I_{D,peak}$ for the discharges run in fixed voltage mode decreases from 76 A to 12 A. For the discharges run in fixed voltage mode, the discharge voltage V_D increases from 510 V to 660 V between the configurations C0E0 and C10E0. A detailed description of these changes are given by Hajihoseini *et al* [8].

2.2. Discharge modelling

We use the IRM to obtain a set of internal discharge parameters that are relevant for our discussion on the discharge physics. The IRM is a global plasma-chemistry model based on energy balance and particle balance and was developed to improve the understanding of the operation of HiPIMS discharges [16, 23]. It models the volume reactions inside the IR and the species interactions with the target surface, as well as the fluxes in and out of the IR such as the sputter flux into the IR and the out-diffusion of working gas and target species [16, 24]. As the IRM is semi-empirical, it needs experimental

input. As in earlier studies [16, 18, 19, 25], this input was the measured discharge current and voltage waveforms as well as the ionized flux fraction measured above the IR. All of these measured values are available for the discharges described in section 2.1.

The IRM gives access to internal discharge parameters that are usually not easily accessible by experiments. Here, in particular, we discuss a sub-group of six internal parameters that are involved in the energy balance in the discharge, namely the discharge voltage V_D, the sheath potential V_{SH}, the potential drop over the ionization region $V_{IR} = V_D - V_{SH}$, the temperatures of the cold and hot electron groups $T_{e,cold}$ and $T_{e,hot}$, respectively, and the power fraction of Ohmic electron heating over the total power to the electrons $P_{Ohm}/(P_{Ohm} + P_{SH})$. Note that the IRM is a global model which uses the approximation that the internal discharge parameters are homogenous inside the considered IR volume. It therefore provides spatially averaged internal discharge parameters that may, in reality, be superimposed by spatial and temporal variations caused by e.g. instabilities such as spokes [26]. The use of a global model also implies that the magnetic field cannot be taken into account explicitly. The magnetic field, in reality, is strongly varying in magnitude and direction within the IR of a magnetron sputtering discharge, which is incompatible with a global approach of plasma parameters being homogeneous in the IR. Therefore, the magnetic field is not modelled explicitly, but rather taken into account indirectly, by using experimentally determined parameters measured under different magnetic configurations, e.g. the ionized flux fraction and the discharge current waveform to fit the model to the discharge.

The IR volume lies above a disc cathode target. It is approximated by a torus with a rectangular cross-section with inner and outer radius r_1 and r_2 and a height $L = z_2 - z_1$, where z_1 is the sheath width, sitting above the racetrack. We lack the data to determine if the height of the IR changes with the magnetic field configuration. Therefore, the assumption of a constant IR volume may not be valid. However, we will show that the discharge parameters obtained from the IRM are largely insensitive to changes in the IR volume. We therefore, in the following, report the values for an IR of $r_1 = 11$ mm, $r_2 = 39$ mm, $z_1 = 2$ mm and $z_2 = 25$ mm, as used in earlier studies using this experimental data set [18, 19, 25]. At the same time, we add uncertainty bars to each data point that give the uncertainty range if the height L of the IR is changed by $\pm 10\%$.

3. Results and discussion

The discharges described in section 2 were controlled by keeping the peak discharge current constant (fixed current mode) or by keeping the discharge voltage constant (fixed voltage mode) while the magnetic field configuration was varied. At the same time, the pulse repetition frequency for all discharges was adjusted in order to keep a constant average power [8]. As the IRM models only single pulses, the pulse repetition frequency is not explicitly modelled. Therefore, for the modelled discharges, there is only one control parameter, that is the peak discharge current for the discharges operated in fixed
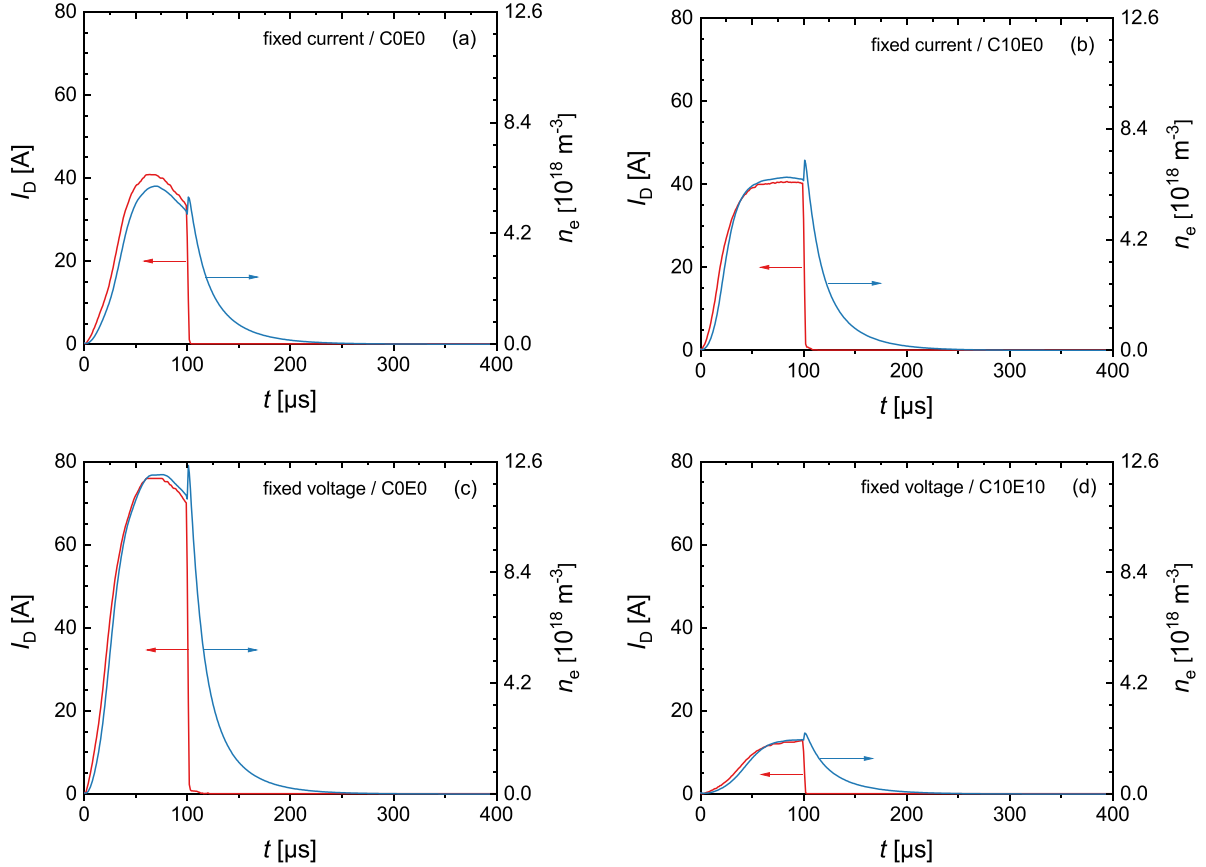
Figure 3. Comparison between the temporal evolution of the discharge current and the electron density determined by the IRM for selected magnetic field configurations and discharge modes. Fixed current mode ($I_{D,peak} \approx 40$ A) for configuration (a) C0E0, and (b) C10E0, and fixed voltage mode for configurations (c) C0E0 ($I_{D,peak} \approx 76$ A), and (d) C10E10 ($I_{D,peak} \approx 12$ A). In all cases the electron density follows closely the discharge current during the 100 μs HiPIMS pulse. Note that the scale for the discharge current I_D and the electron density n_e does not change between panels.

current mode or the discharge voltage for the discharges operated in fixed voltage mode. Keeping one or the other of these two adjustable control parameters constant reveals different aspects of the discharge physics, as discussed in the following.

In section 3.1 we begin our analysis by studying how the peak discharge current influences the electron density n_e in the IR. This is followed by unravelling the reasons for the variations of the discharge voltage in the case of the fixed current discharges and the peak discharge current in the case of the fixed voltage discharges. To explore this, in section 3.2, we look at how a sub-group of internal discharge parameters varies with the magnetic field. The reason for using a HiPIMS process for thin film deposition is the enhanced probability of target species ionization. In section 3.3, we therefore discuss the variations of the probability of target species ionization in view of the variation of the internal discharge parameters discussed in the preceding sections.

3.1. Influence of the magnetic field and the discharge current on the electron density

Let us first analyze how the discharge current influences the electron density n_e. Figure 3 shows the temporal evolution of the discharge current and the electron density n_e within the

IR, as determined by the IRM for four cases: two in fixed peak current (40 A) mode and two in fixed voltage (625 V) mode. We see that the evolution of the $n_e(t)$ and $I_D(t)$ curves follow each other rather closely during the entire pulse-on time. They can be approximated quite well by

$$n_e = 1.6 \times 10^{17} \times I_D, \tag{1}$$

where I_D is in (A) and n_e is in (m^{-3}). An evaluation for all the experimental data (not shown) shows that this approximation holds equally well independent of the magnetic field configuration, the applied discharge voltage and current, and during all times within the HiPIMS pulse. Using the surface area of the target, $S_{target} = \pi r_{target}^2 = 8.1 \times 10^{-3}$ m^2, equation (1) can be expressed in terms of current density, $J_{D,target}$ (A m^{-2}), averaged over the entire target surface S_{target},

$$n_e = 1.3 \times 10^{15} \times J_{D,target}. \tag{2}$$

Figure 3 shows that after the end of the pulse, the discharge current rapidly drops to zero. The electron density decays more slowly, though. The trajectory of ions to the cathode target is not influenced by the magnetic field, but by a potential in the pre-sheath region that leads to ion back-attraction. When the pulse ends, ion back-attraction disappears, and the ions can
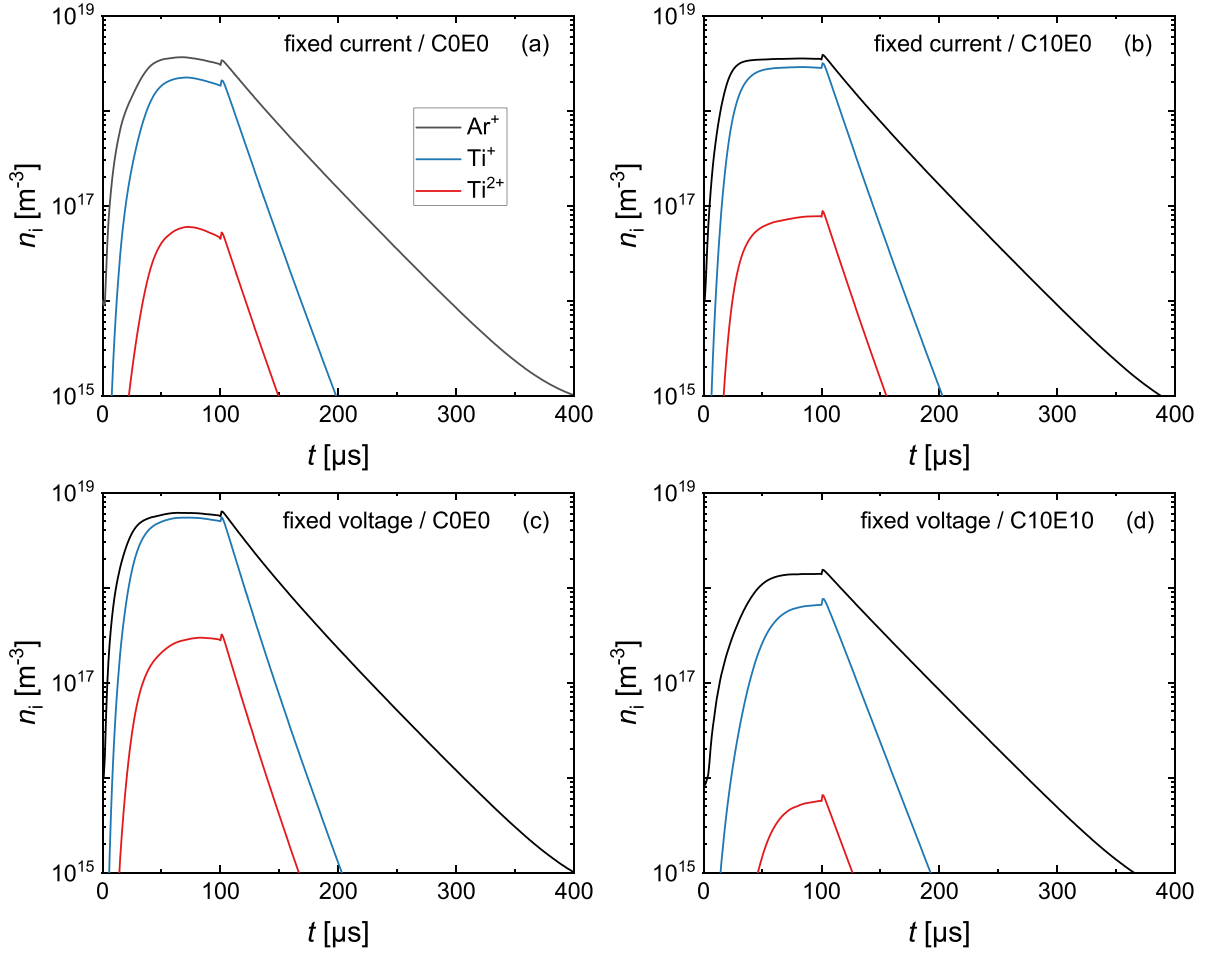
J. Phys. D: Appl. Phys. **55** (2022) 015202

M Rudolph *et al*

Figure 4. The temporal evolution of the ion densities determined by the IRM for selected magnetic field configurations and discharge modes. Fixed current mode ($I_{\mathrm{D,peak}} \approx 40$ A) for configuration (a) C0E0, and (b) C10E0, and fixed voltage mode for configurations (c) C0E0 ($I_{\mathrm{D,peak}} \approx 76$ A), and (d) C10E10 ($I_{\mathrm{D,peak}} \approx 12$ A).

freely leave to the diffusion region [15, 18]. We propose that the decay rate of the plasma density is determined by this ion loss. However, maintenance of quasineutrality demands that ions and electrons leave the magnetic trap region at the same rate. Consequently, the electrons easily leave the IR, at a rate limited to maintain quasineutrality, by motion along the magnetic field lines. The temporal evolution of the ion densities determined by the IRM for selected magnetic field configurations and discharge modes is shown in figure 4. In all cases the Ar$^+$ ion has the highest density, the Ti$^+$ density is always somewhat smaller, and the Ti^{2+} density is always at least an order of magnitude smaller. In fact, the highest Ti^{2+} ion density observed is 2.7% of the total ion density and is reached for the discharge run in fixed voltage mode with the magnetic field configuration C0E0. The Ti$^+$ ions appear later than the Ar$^+$ ions and the Ti^{2+} ions appear the latest. The decay rate of the Ti$^+$ is faster than for the Ar$^+$ ions.

The resemblance between the time-evolution of $n_{\mathrm{e}}(t)$ and $I_{\mathrm{D}}(t)$ during the HiPIMS pulse has been observed before experimentally by Held *et al* [27]. It can be understood by equalizing the discharge current with the ion current to the target. We note that at the target surface the discharge current density is usually normalized to the racetrack surface area S_{RT}.

At the target surface the discharge current is mainly carried by ions from the IR, neglecting the contribution from secondary electrons, the current density is given by Huo *et al* [16]:

$$J_{\mathrm{D,RT}}(t) \approx \frac{I_{\mathrm{ion}}^{\mathrm{RT}}(t)}{S_{\mathrm{RT}}} = \sum_k \frac{e a_k n_k(t)(z_2 - z_1)\beta_{\mathrm{pulse}}}{t_{\mathrm{loss},k}}, \quad (3)$$

where k denotes the ion species ($k = \mathrm{Ar}^+, \mathrm{Ti}^+, \mathrm{Ti}^{2+}$), e is the elementary charge, and $I_{\mathrm{ion}}^{\mathrm{RT}}(t)$ is the time-dependent ion current to the racetrack. As ion species, here, we take Ar$^+$, Ti$^+$ and Ti^{2+}, because these are modelled in the IRM. On the right hand side, a_k is the charge state of ion species k, $n_k(t)$ is their density in the IR, $t_{\mathrm{loss},k}$ is their loss time out of the IR, and β_{pulse} is the probability of ion back-attraction to the target during the pulse [18]. The loss time for ion species k can be approximated by [16]

$$t_{\mathrm{loss},k} = \frac{z_2 - z_1}{\sqrt{a_k e V_{\mathrm{IR}}/m_k}}, \quad (4)$$

where $L = z_2 - z_1$ is the height of the IR above the sheath edge, V_{IR} is the potential drop over the IR and m_k is the mass of ion species k. Sheridan *et al* [28] argue that since electrons

and ions are created at almost the same rate, their confinement time must be roughly the same and consequently $t_{\text{loss},k} \propto \sqrt{m_k}$, given that the magnetic geometry and the ionization profile remains fixed. We here note that we find the same proportionality in equation (4). We enter $t_{\text{loss},k}$ from equation (4) into equation (3), and move out constant terms from the summation, giving

$$J_{\text{D,RT}}(t) = e^{3/2} \sum_k a_k^{3/2} n_k(t) \beta_{\text{pulse}} \sqrt{\frac{V_{\text{IR}}}{m_k}}. \tag{5}$$

Let us evaluate equation (5) for a 'typical ion, in a typical discharge'. From previous IRM runs, we know that β_{pulse} lies in the range 0.87–0.93 [25] and we here use the mean value $\beta_{\text{pulse}} = 0.9$. The value of V_{IR} varies between 36 and 50 V for the present discharges (see figure 6(a) below). Here, we use a mean value of $V_{\text{IR}} = 43$ V. Furthermore, we replace all three ionic species by a single species with charge state $a_k = 1$ which is justified because only a few percent ($<3\%$ of the ion density) of doubly charged ions (Ti^{2+}) are present in the discharge (see figure 4). We also use a single value for the mass $m_k = A_k m_{\text{p}} = 44\, m_{\text{p}}$, where m_{p} is the proton mass, which lies between the masses of argon $A_{\text{Ar}} = 39.9\, m_{\text{p}}$ and titanium $A_{\text{Ti}} = 47.9\, m_{\text{p}}$. Moving out all constants from the summation in equation (5), and resolving n_{e} to the left, yields

$$n_{\text{e}}(t) = \sum_k n_k(t) = 7.2 \times 10^{14} \times J_{\text{D,RT}}(t), \tag{6}$$

where n_{e} is in (m^{-3}) and $J_{\text{D,RT}}$ is in (A m^{-2}) and where we have used the condition of quasi-neutrality to replace $\sum_k n_k$ with n_{e}. Using $J_{\text{D,RT}} = (S_{\text{target}}/S_{\text{RT}}) J_{\text{D,target}}$ with $S_{\text{target}} = 8.1 \times 10^{-3}$ m^2 and $S_{\text{RT}} = \pi(r_2^2 - r_1^2) = 4.4 \times 10^{-3}$ m^2 we obtain the relation between n_{e} and the current density normalized to the entire target surface area,

$$n_{\text{e}}(t) = \sum_k n_k(t) = 1.3 \times 10^{15} \times J_{\text{D,target}}(t). \tag{7}$$

This result for a 'typical ion, in a typical discharge' agrees well with the empirical approximation of equation (2). The small deviations in figure 3 from an exact proportionality between n_{e} and J_{D} can be understood from the variations of the parameters β_{pulse}, V_{IR}, and m_k around the assumed typical values. Here, the slight deviation of the electron density from the discharge current for the discharge run in fixed current mode and using the magnetic field configuration C0E0 (figure 3(a)) compared to that with the magnetic field configuration C10E0 (figure 3(b)) are mainly due to a variation in V_{IR}. For the magnetic field configuration C0E0, $V_{\text{IR}} = 50.5$ V, and for the configuration C10E0, $V_{\text{IR}} = 40.9$ V (see figure 6(a)). This difference results in a 10% lower electron density for the configuration C0E0 compared to the configuration C10E0 in fixed current mode. Similarly, the discharges run in fixed voltage mode with the magnetic field configurations C0E0 and C10E10 clearly have a very different peak discharge current ($I_{\text{D,peak}} = 76$ A and 12 A, respectively) and, therefore, exhibit a different composition

of the ion current at the target surface. Here, for Ar and Ti with very similar masses, the proportionality factor between n_{e} and $J_{\text{D,target}}$ changes only by $\pm5\%$ between the two extreme cases of a pure Ar$^+$ current compared to a pure Ti$^+$ current.

Measurements of the electron density in HiPIMS discharges have been made over the years. A compilation of peak electron densities normalized to the peak discharge current density (averaged over the entire target) for various HiPIMS discharges and target materials (Ti, Cu, Cr, Al, C, Ta, Nb, and W) has been made by Čada *et al* [29]. All discharges in that compilation were operated with argon as the working gas over a range of pressures (0.27–2.7 Pa) and it is found that with variations of the process conditions (pressure, target size, and target material), the pulse configuration, and the exact location of the probe measurement in the discharge, $n_{\text{e}}/J_{\text{D,peak}}$ varied in the range 3.0×10^{13}–1.5×10^{15} (Am)$^{-1}$ [29]. Our results (equation (2)) lie at the upper border of what has been observed experimentally, which may be explained by the measurements not being made close to the target, i.e. in the most intense part of the discharge, where probe measurements are typically difficult to do. The reported experimental electron densities are therefore often lower compared to the here-presented values from the IRM. Taking these experimental challenges into account, in general, the agreement between experiments and modelling seems acceptable. It suggests that the close link between the electron density and the discharge current is a fundamental relation with a validity that goes beyond the discharges under investigation here. It is therefore concluded that, for any given discharge current, neither the magnetic field strength nor the degree of magnetic unbalance has any significant influence on the electron density. The principal influence on the electron density is from the discharge current, and here the relation is a simple proportionality.

3.2. Influence of the magnetic field on the electron temperature and Ohmic heating

In the preceding section we have learned that, independent of both the magnetic field configuration and the time during the pulse, the electron density in the IR closely follows the discharge current. In our case this relation $n_{\text{e}}(I_{\text{D}})$ is given by equation (1). The experimentalist can therefore select any desired electron density by adjusting the discharge current. The electron density is to a large extent determined by the rate coefficient for electron impact ionization, which in turn is determined by the electron temperature. The following section is therefore an analysis of how the electron heating and the electron temperature change with varying magnetic field configuration and discharge current.

Let us first discuss the two externally measured discharge parameters that are involved, the discharge voltage and current. Figure 5 gives the variations of discharge voltage and current with the magnetic field parameter z_{gap}. Remember that the parameter z_{gap} is an empirical parameter that represents changes in the magnetic field configuration. Despite its ad-hoc nature and simplicity, it seems to capture quite well the
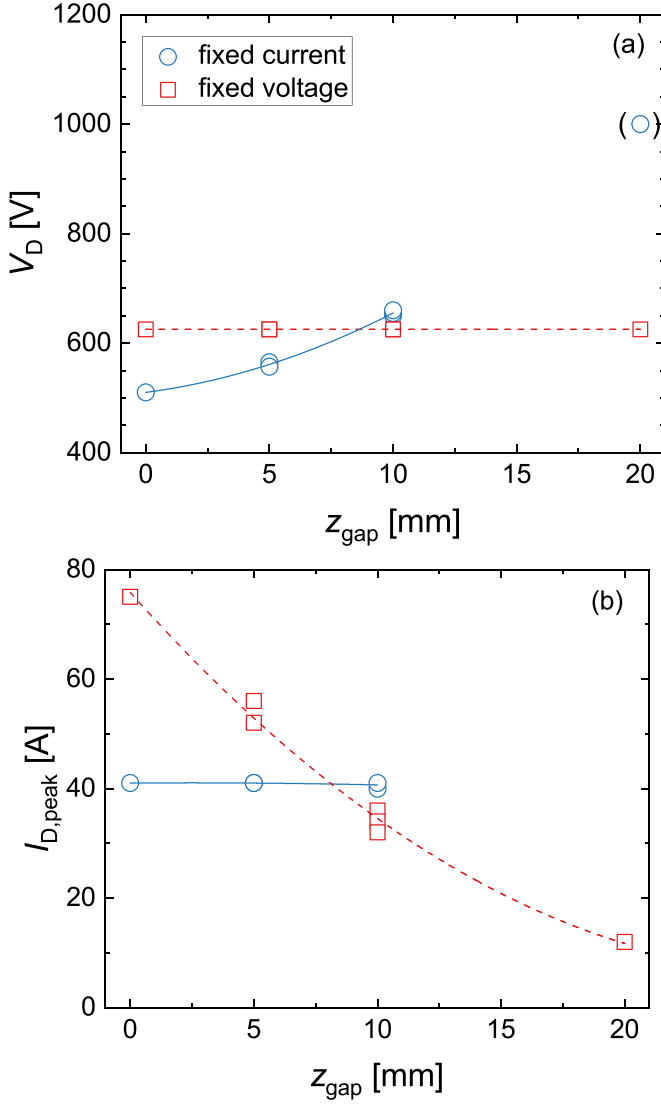
Figure 5. (a) The discharge voltage V_D, and (b) the peak discharge current $I_{D,peak}$, as a function of the empirical parameter z_{gap} for the discharges run in fixed current and fixed voltage mode. Note, that the data point in parenthesis indicates a lower boundary for the discharge voltage, as the discharge did not reach the required peak discharge current of 40 A at the maximum output voltage of the used pulsing unit. The lines are 2nd order polynomial fits to the data points.

essence of the magnetic field configuration. This can be seen by considering the trends in either fixed current mode or fixed voltage mode, where very different magnetic field configurations have a similar discharge voltage as shown in figure 5(a) and a similar discharge current as shown in figure 5(b), if the parameter z_{gap} has the same value. That applies to the magnetic field configurations (C0E5, C5E0) and (C0E10, C5E5, C10E0) with values of $z_{gap} = 5$ mm and $z_{gap} = 10$ mm, respectively. Keep in mind that the discharge voltage, the discharge current, and z_{gap} are experimentally determined parameters and independent of any model, which gives us confidence that the parameter z_{gap} carries a physical meaning.

There is in figure 5, both for the fixed current and for the fixed voltage cases, a common trend: for smaller values of z_{gap},

the discharge delivers 'more current per voltage'. Huo *et al* [16] discuss the relation between discharge current, discharge voltage and magnetic field strength. They define an effective discharge impedance as $R_{eff} = V_D/I_{D,peak}$, and report a decreasing R_{eff} with increasing magnetic field. Since a smaller z_{gap} is correlated to stronger magnetic fields (figure 1) this is consistent with our findings here: the discharges with a lower value of z_{gap} exhibit a lower effective discharge impedance R_{eff}. As an entry to the analysis below we can note that this is somewhat counterintuitive, since a stronger B-field leads to a lower electron mobility across the magnetic field lines [30, 31]. One could, therefore, expect that a higher discharge voltage would be needed to drive the electron current across a stronger magnetic field, and thus result in a higher R_{eff}. Let us call the observed opposite trend the 'apparent voltage paradox'.

For a deeper insight, we have from the IRM-runs extracted how four internal discharge parameters vary as functions of the magnetic field parameter z_{gap}. The parameters that we will look at are the sheath potential V_{SH}, the potential drop over the IR, $V_{IR} = V_D - V_{SH}$, and the temperatures describing the cold and hot electron groups $T_{e,cold}$ and $T_{e,hot}$, respectively. The trends of these parameters with z_{gap} are shown in figure 6.

The potential drop over the IR, V_{IR}, as well as the cathode sheath voltage, V_{SH}, are presented in figures 6(a) and (b), respectively. V_{IR} shows quite a similar trend for the discharges run in fixed current and fixed voltage modes. In both cases, it decreases with increasing z_{gap} (which, again, is correlated to weaker magnetic fields). This observation is in line with experimental probe measurements by Mishra *et al* [17] who reported a smaller potential drop over the IR for weaker magnetic fields. For V_{SH}, the trends for the two modes are similar in the sense that both are rising, but they are dissimilar in strength. While the fixed voltage cases have only a small increase of V_{SH}, the fixed current cases show a strongly increasing V_{SH}, with increasing parameter z_{gap}. For both discharge modes, the V_{SH} curves in figure 6(b) strongly resemble the V_D curves in figure 5(a). This is not the case for the V_{IR} curves. For the discharges run in fixed current mode, V_{IR} even shows the opposite trend: despite a rising discharge voltage in figure 5(a) with increasing z_{gap}, V_{IR} decreases as shown in figure 6(a).

The trends in V_{IR} for both discharge modes are mimicked by the temperature of the cold electron group (compare figures 6(a) and (c)). This can be explained by Ohmic heating that depends on the potential drop over the IR, V_{IR}. Most of the power delivered to Ohmic heating is used to heat cold electrons, simply because they have a much higher number density compared to the hot electron group [19]. Similarly, the trends in V_{SH} for both discharge modes are mimicked by the temperature of the hot electron group (compare figures 6(b) and (d)). This observation can be explained by the hot electrons gaining their energy in the cathode sheath and that the energy gain corresponds to exactly the sheath voltage V_{SH}.

The coupling between the three discharge parameters V_D, V_{IR}, and V_{SH} can be understood as a combination of particle balance and energy balance. In order for the plasma to remain quasi-neutral, the loss rates of ions and electrons from the IR
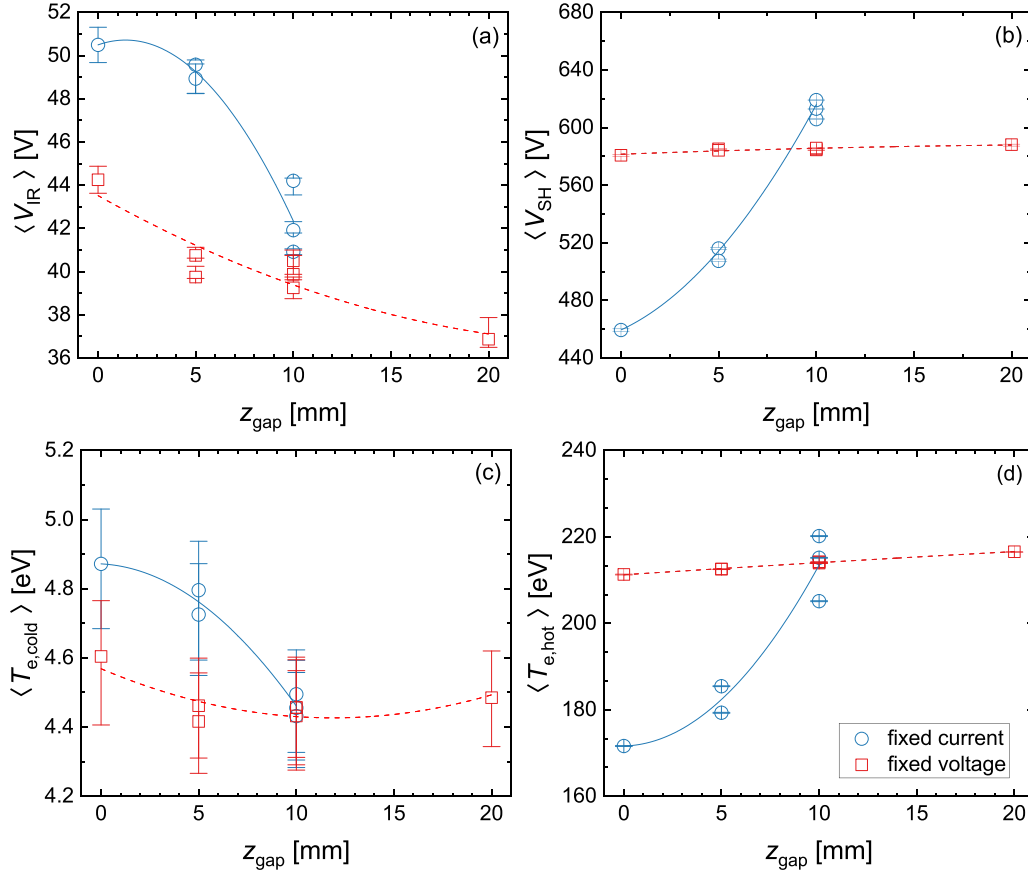
Figure 6. IRM-derived discharge parameters: (a) potential drop over the IR V_{IR}, (b) cathode sheath potential drop V_{SH}, (c) temperature of the cold electron group, and (d) temperature of the hot electron group. The uncertainty bars indicate the range of parameters obtained by varying the IR height by $\pm 10\%$. The hot electron temperature does not depend on changes in the height of the IR. All parameters are averaged over the pulse length. The reported parameter values are averaged over one pulse.

during the pulse have to be identical, the ions going mainly to the target and the electrons to the diffusion region. For simplicity we now consider the fixed current discharges only, and the effects of a decrease in the parameter z_{gap}. This scales approximately with a stronger magnetic field as can be seen in figure 2. The Pedersen conductivity governs the current along the axial electric field that is transverse to the magnetic field (electron cross-**B**), while the Hall conductivity determines the current perpendicular to both the magnetic and the electric fields [32, section 5.3]. For a stronger magnetic field, the electron Pedersen cross-**B** mobility decreases [30, 33], and a higher potential drop V_{IR} therefore becomes necessary to give the same electron cross-**B** drift speed towards the diffusion region. This higher IR potential drop is seen in figure 6(a), and it brings the energy balance into the picture because it increases the rate of Ohmic heating of electrons [16], and thereby gives a higher (cold) electron temperature $T_{e,cold}$, as can be seen in figure 6(c). This, in turn, reduces the need for a high ionization rate from the hot electron population. The fixed discharge current can therefore, at lower z_{gap}, be maintained at a lower sheath voltage, as seen in figure 6(b), and a lower hot electron temperature, as seen in figure 6(d).

Figure 7 shows the power dissipation channels for three fixed current discharges with different values of z_{gap}. The surface area of the pies indicates the pulse power, i.e. the electrical energy dissipated during one pulse divided by the pulse length [34],

$$\langle P_{pulse} \rangle = \frac{1}{t_{pulse}} \int_{t_{pulse}} I_D(t) V_D(t) \mathrm{d}t, \tag{8}$$

where t_{pulse} is the pulse length. One can see that most of $\langle P_{pulse} \rangle$, or $\geqslant 93\%$, is used to accelerate ions, mostly across the cathode sheath, and this power is finally dissipated in the target as heat. For the discharge with magnetic field configuration C0E0 ($z_{gap} = 0$), 7% of the pulse power is absorbed by the electrons and this fraction decreases for higher values of z_{gap}, indicating a shift to less energy-efficient discharges. In other words, for an increasing magnetic field parameter z_{gap}, more energy is spent on heating up the target.

The parameter $P_{Ohm}/(P_{Ohm} + P_{SH})$ can similarly be regarded as a measure for energy efficiency of a discharge. This is because a higher fraction of Ohmic heating over total electron energization ($P_{Ohm} + P_{SH}$) will always have a lower $\langle P_{pulse} \rangle$ because Ohmic heating of electrons is accompanied by
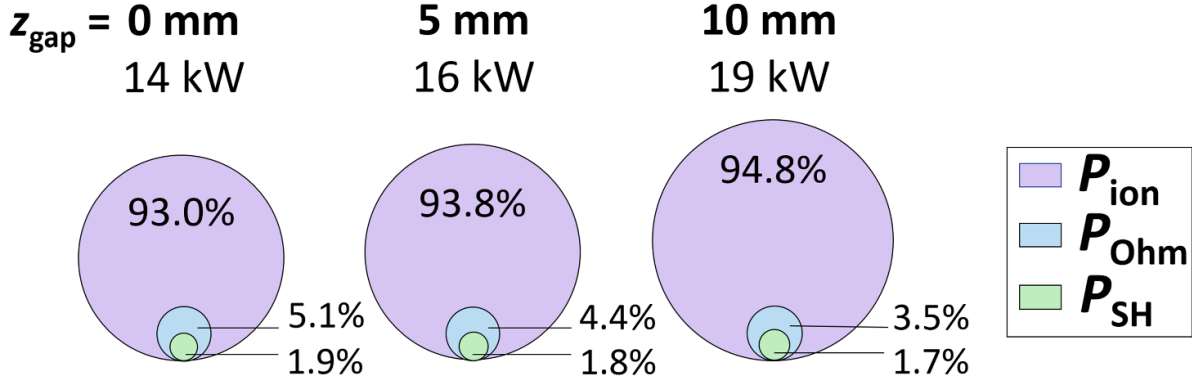
Figure 7. Fractions of pulse power for fixed current discharges with different values of z_{gap} that are used for ion acceleration (P_{ion}), Ohmic heating (P_{Ohm}), and sheath energization (P_{SH}). The power (in (kW)) stated above each diagram is the pulse power $\langle P_{pulse} \rangle$ defined in the text.
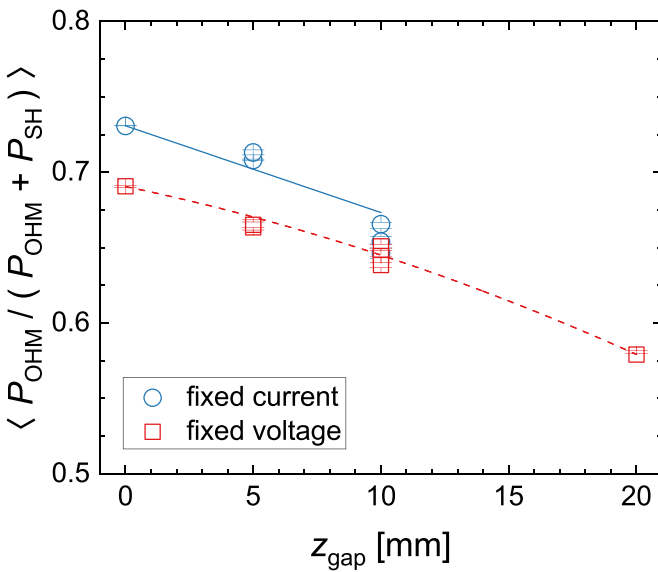

Figure 8. Share of power to the electrons that goes to Ohmic heating versus the magnetic field parameter z_{gap}.

less ion heating compared to sheath energization of electrons. This is the reason why both measures of efficiency, the fraction of total power that goes to electron heating, and the electron-energizing fraction of the power that goes to Ohmic heating, $P_{Ohm}/(P_{Ohm} + P_{SH})$, are equivalent. $P_{Ohm}/(P_{Ohm} + P_{SH})$ is plotted versus the magnetic field parameter z_{gap} in figure 8. It shows that for increasing magnetic field parameter z_{gap}, the fraction $P_{Ohm}/(P_{Ohm} + P_{SH})$ decreases, in line with the increase in pulse power, as seen in figure 7.

The difference in discharge efficiency also solves the 'apparent voltage paradox' described above. A much higher fraction of power dissipated in the IR, $\frac{1}{t_{pulse}} \int_{t_{pulse}} I_D(t) V_{IR}(t) \, dt$, is used to heat electrons, compared to the fraction of the power dissipated in the sheath, $\frac{1}{t_{pulse}} \int_{t_{pulse}} I_D(t) V_{SH}(t) \, dt$. Therefore, for the fixed current discharges, to reach the same peak discharge current, the decrease in sheath potential can be more than an order of magnitude larger than the simultaneous increase in the potential drop over the IR for decreasing parameter z_{gap} (compare figures 6(a) and (b)).

In figure 8, we also added the fraction $P_{Ohm}/(P_{Ohm} + P_{SH})$ for the fixed voltage cases. As a sidenote, we observe that the values for the fixed current and the fixed voltage cases are very close to each other despite the differences in peak discharge currents and voltages. This may suggest a fundamental influence of the magnetic field on the fraction $P_{Ohm}/(P_{Ohm} + P_{SH})$.

We conclude that a higher value of z_{gap} indeed decreases the cold electron temperature and increases the hot electron temperature, even if the variations are limited. A much stronger effect of z_{gap}, however, is seen on the electron power absorption mechanism. Here, a lower z_{gap} shifts the electron energization towards Ohmic heating, which is accompanied by less ion heating compared to sheath energization. As a result, for the fixed discharge current mode, the discharge requires less energy per pulse to obtain a desired electron density.

3.3. The probability of target species ionization

Above, we have discussed how the discharge current influences the electron density (section 3.1) while the magnetic field changes the electron heating mechanism and by that the electron temperature (section 3.2). Here, we will discuss the combined influence on one of the key parameters of a HiPIMS discharge, the probability of target species ionization α_t. It is defined as [25]

$$\alpha_t = 1 - \frac{\int_T \Gamma_{tn}^{DR} dt}{\int_T \Gamma_{sput} dt}, \tag{9}$$

where the integration is performed over one period T, i.e. over the pulse and afterglow, Γ_{tn}^{DR} is the flux of metal neutrals from the IR to the diffusion region and Γ_{sput} is the flux of sputtered metal neutrals into the IR due to sputtering. We will analyze how the magnetic field configuration influences the value of α_t. Note that α_t generally varies within the pulse and we here focus on the pulse-averaged values. We furthermore maintain the HiPIMS pulse length constant at $100 \, \mu s$, since α_t may vary with the pulse length, even when the peak discharge current is fixed [35].

There are four processes that are modelled in the IRM, which can lead to target species ionization. These are electron
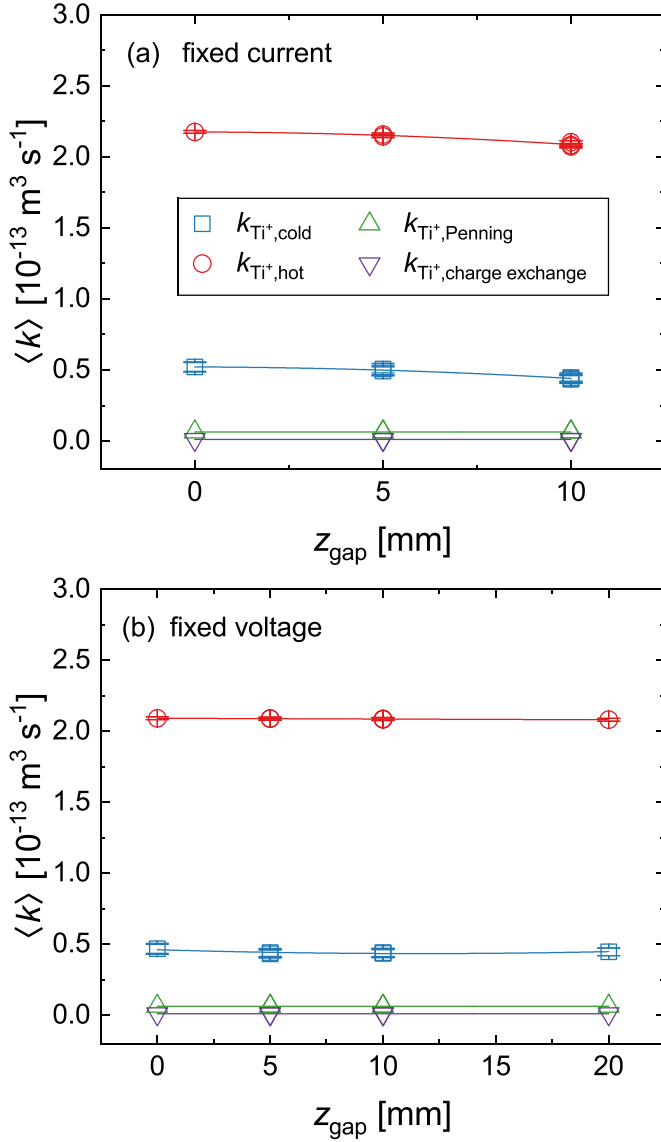
J. Phys. D: Appl. Phys. **55** (2022) 015202

M Rudolph *et al*

Figure 9. Ti ionization rate coefficients for different processes: ionization from collisions with electrons from the cold and the hot electron group ($k_{Ti^+,cold}$ and $k_{Ti^+,hot}$), Penning ionization from Ar^m levels and charge exchange collisions with Ar^+. Panel (a) shows results for discharges run in fixed current mode, panel (b) shows results from discharges run in fixed voltage mode. All rate coefficients are averaged over one pulse.

Figure 10. (a) The probability of target species ionization α_t as a function of z_{gap}, and (b) the probability of target species ionization α_t as a function of peak discharge current $I_{D,peak}$. The dashed line is a fit to the data points and results in the displayed equation. The best fits to the data points are given by the constants $k_1 = 3.3 \times 10^{-2}$ (A^{-1}), $k_2 = 4.7 \times 10^{-2}$ (A^{-1}) and $k_3 = 3.3 \times 10^{-4}$ (A^{-2}).

impact ionization from the cold and the hot electron populations, Penning ionization from collisions between neutral Ti and Ar^m and charge exchange collisions between neutral Ti and Ar^+ [16]. Ionization to form the doubly charged Ti^{2+} is neglected in the discussion here (although included in the IRM calculations). Of these processes, the most important is electron impact ionization by the cold electrons [19], because they have the highest density. To evaluate the impact of each ionization process in more detail, the pulse-averaged rate coefficients for the four processes for the fixed current and the fixed voltage cases are shown in figures 9(a) and (b), respectively. One can see that the rate coefficients vary by only ~10% with varying magnetic field parameter z_{gap}, despite the variations
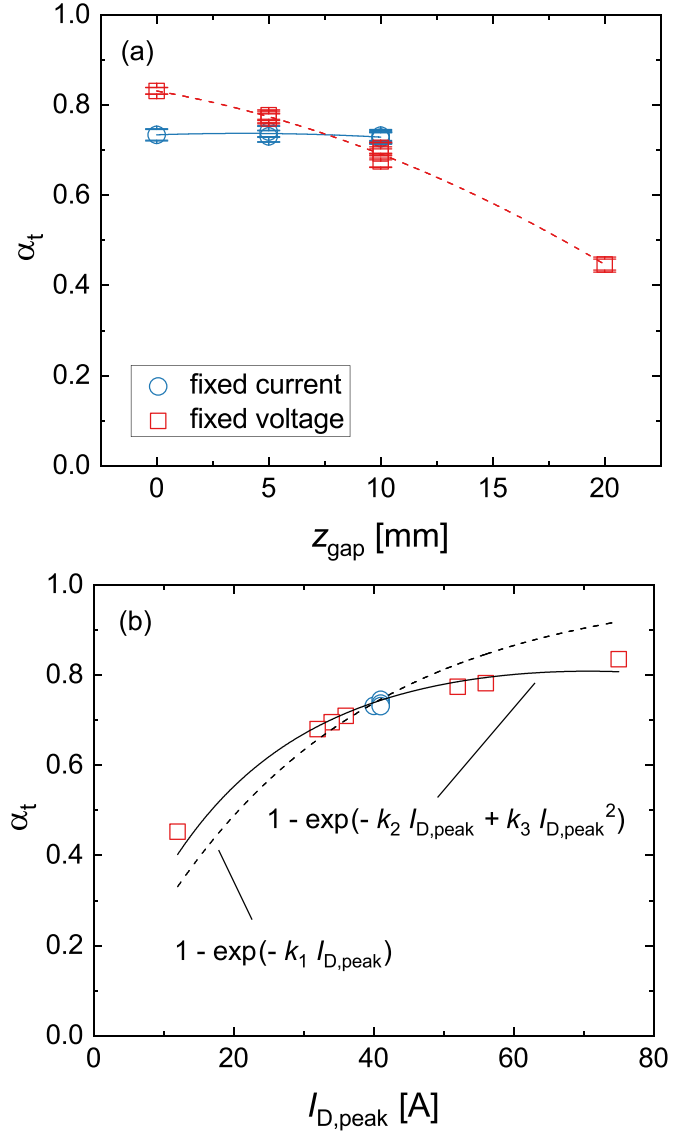
in the temperatures of the hot and cold electron group. For the discharges run in fixed current mode this, in combination with the close to constant electron density (figures 3(a) and (b)), means that a constant fraction of the sputtered atoms is ionized. Figure 10(a) summarizes the variation of α_t as a function of the parameter z_{gap}. In fixed current mode, the probability of ionization remains constant. For the discharges run in fixed voltage mode, we note that the ion density, and to obey quasi-neutrality, also the electron density vary substantially (figures 3(c) and (d)). As a result, the probability of ionization of target species varies by the same amount.

At first glance the results shown in figure 10(a) appear contradictory as a variation of one of the key discharge parameters, the magnetic field, has no influence on the probability of

target species ionization α_t in the fixed discharge current case. However, as discussed in section 3.1, an almost constant peak electron density n_e is a result of the constant peak discharge current. To test if n_e (rather than the magnetic configuration) is the key parameter for α_t, we plot α_t as a function of $I_{D,peak}$, for the discharges run in fixed current and in fixed voltage mode (figure 10(b)). It gives a smooth curve that is steep at low discharge currents and levels off at high discharge currents.

The shape of the curve of α_t vs. $I_{D,peak}$ can be understood by considering a Ti atom sputtered off the target and passing through the IR. The probability of an ionizing collision with an electron is then

$$F_{ion} = 1 - \exp\left(-\frac{t_{cross}}{t_{Ti^+}}\right), \tag{10}$$

where t_{cross} is the average time it takes a sputtered atom to cross the IR and $t_{Ti^+} = 1/(n_e k_{Ti^+})$ is the average time for ionization, and k_{Ti^+} is the electron impact rate coefficient for ionization of the Ti atom. As the electron density varies during the pulse, t_{Ti^+} varies with time during the pulse. The highest density of sputtered atoms is found at the time the current peaks [18]. Here we approximate $t_{Ti^+} = 1/(n_{e,peak} k_{Ti^+})$. Assuming a constant crossing time, using equation (1), and summarizing all constant values (including k_{Ti^+} that varies only little with $I_{D,peak}$, see figure 9) into a constant k_1, we obtain (see appendix A)

$$F_{ion} = 1 - \exp\left(-k_1 I_{D,peak}\right). \tag{11}$$

A dashed line in figure 10(b) shows a fit of the data points to equation (11) with $k_1 = 3.3 \times 10^{-2}$ (A^{-1}). The fit in general reflects the trend of α_t from which we conclude that the rising electron density from an increasing peak discharge current is the primary driver for the higher probability of ionization. However, we also note that the curve in figure 10(b) is slightly too steep and that a secondary effect is likely superimposed. We suggest that this secondary effect is gas rarefaction. At higher discharge currents, a higher degree of rarefaction can be expected which would decrease t_{cross} because, on average, sputtered atoms then experience fewer collisions within the IR. Assuming a linear variation of t_{cross} with $I_{D,peak}$ and summarizing again all the constants gives (see appendix A)

$$F_{ion} = 1 - \exp\left(-k_2 I_{D,peak} + k_3 I_{D,peak}^2\right). \tag{12}$$

A fit of the data points to equation (12) is shown in figure 10(b) by a solid line. The fit shows an almost perfect match with the data points with the constants $k_2 = 4.7 \times 10^{-2}$ (A^{-1}) and $k_3 = 3.3 \times 10^{-4}$ (A^{-2}). We therefore note that rarefaction is to be considered as a secondary effect to explain the shape of α_t with $I_{D,peak}$. This has consequences as the increase in electron density and the increased degree of rarefaction with $I_{D,peak}$ have opposing effects on α_t. The gas rarefaction at high $I_{D,peak}$ dampens the increase of α_t.

Remember that the primary influence of α_t is the variation of $n_{e,peak}$ caused by a varying $I_{D,peak}$. Due to the close link between $n_e(t)$ and $I_D(t)$, discussed in section 3.1, the probability of ionization α_t can be well adjusted by varying the external process parameter $I_{D,peak}$. This was qualitatively already shown by Brenning *et al* [35].

4. Summary

We discuss the influence of the magnetic field on the electron density and electron temperature, which, in turn, determine the probability of target species ionization α_t in a HiPIMS discharge. To quantify the effect of changes in the magnetic field strength and the degree of magnetic unbalance, we define an empirical magnetic field parameter that consists of summing the distances of the two magnet packs from the rear surface of the target. We denote this parameter z_{gap}.

We find that the electron density closely follows the discharge current during the HiPIMS pulse, while the magnetic field only indirectly influences the electron density via the discharge current. On the other hand, *the magnetic field has a large influence on the electron power absorption mechanism.* The closer the magnets are to the target (smaller z_{gap}) the higher is the fraction of the total power that goes to electron energization, and the higher is the fraction of total electron energization that goes to Ohmic heating, i.e. electron energization in the potential drop across the IR. As a result, the cold electron temperatures are higher, and the hot electron temperatures are lower, when the magnets are close to the target.

Overall, however, the variation in the electron temperature remains too small to significantly influence the rate coefficients for target species ionization. This results in the probability of target species ionization being primarily dependent on the electron density, and thereby largely independent of the magnetic field strength. As the peak discharge current controls the electron density in the ionization region, it can be used to adjust the probability of target species ionization. At high peak discharge currents, the probability of ionization saturates at a level well below unity, which is an effect of gas rarefaction. With increasing degree of gas rarefaction at high peak discharge currents, the time for metal atoms to cross the IR becomes shorter due to fewer collisions with the rarefied argon working gas. This reduced residence time for sputtered metal atoms in the IR hampers electron impact collisions and results in a saturation of the probability of ionization with increasing peak discharge current.

Data availability statement

The data that support the findings of this study are available upon reasonable request from the authors.

Acknowledgments

Appendix A. Ionizing collisions

In section 3.3 the probability of target species ionization is discussed and related to the discharge current. In the following, we will derive equations (11) and (12). Starting with equation (10) and using $t_{Ti^+} = 1/(n_{e,peak}k_{Ti^+})$ from the discussion above, yields

$$F_{ion} = 1 - \exp\left(-t_{cross}n_{e,peak}k_{Ti^+}\right). \quad (A.1)$$

Using now $k_1 = 1.6 \times 10^{17} \times t_{cross}k_{Ti^+}$ where the numerical factor is from equation (1), yields

$$F_{ion} = 1 - \exp(-k_1 I_{D,peak}), \quad (A.2)$$

which is the sought equation (11).

Equation (12) can be derived in a similar manner. Using equation (A.1) and entering a linear variation of t_{cross} with $I_{D,peak}$, i.e. $t_{cross} = t_0(1 - k_{rare}I_{D,peak})$, where t_0 is the crossing time without any rarefaction and k_{rare} is a proportionality constant, yields

$$F_{ion} = 1 - \exp\left(-\frac{t_0 k_1 I_{D,peak}}{t_{cross}} + \frac{t_0 k_1 k_{rare}I_{D,peak}^2}{t_{cross}}\right). \quad (A.3)$$

Summarizing again the constants into $k_2 = t_0 k_1/t_{cross}$ and $k_3 = t_0 k_1 k_{rare}/t_{cross}$ yields equation (12).

ORCID iDs

M Rudolph https://orcid.org/0000-0002-0854-6708
N Brenning https://orcid.org/0000-0003-1308-9270
H Hajihoseini https://orcid.org/0000-0002-2494-6584
T M Minea https://orcid.org/0000-0003-2886-3492
A Anders https://orcid.org/0000-0002-5313-6505
J T Gudmundsson https://orcid.org/0000-0002-8153-3209
D Lundin https://orcid.org/0000-0001-8591-1003

References

[1] Gudmundsson J T 2020 *Plasma Sources Sci. Technol.* **29** 113001
[2] Kelly P J and Arnell R D 2000 *Vacuum* **56** 159
[3] Waits R K 1978 *J. Vac. Sci. Technol.* **15** 179
[4] Chapin J S 1974 *Res. Dev.* **25**(1) 37
[5] Krüger D, Köhn K, Gallian S and Brinkmann R P 2018 *Phys. Plasmas* **25** 061207
[6] Bradley J W, Mishra A and Kelly P J 2015 *J. Phys. D: Appl. Phys.* **48** 215202
[7] Alami J, Stranak V, Herrendorf A-P, Hubicka Z and Hippler R 2015 *Plasma Sources Sci. Technol.* **24** 045016
[8] Hajihoseini H, Čada M, Hubička Z, Ünaldi S, Raadu M A, Brenning N, Gudmundsson J T and Lundin D 2019 *Plasma* **2** 201
[9] Kolev I, Bogaerts A and Gijbels R 2005 *Phys. Rev.* E **72** 056402
[10] Bultinck E and Bogaerts A 2009 *New J. Phys.* **11** 103010
[11] Bradley J W, Thompson S and Gonzalvo Y A 2001 *Plasma Sources Sci. Technol.* **10** 490
[12] Ryabinkin A N, Serov A O, Pal A F, Mankelevich Y A, Rakhimov A T and Rakhimova T V 2021 *Plasma Sources Sci. Technol.* **30** 055009
[13] Gudmundsson J T and Hecimovic A 2017 *Plasma Sources Sci. Technol.* **26** 123001
[14] Brenning N, Gudmundsson J T, Lundin D, Minea T, Raadu M A and Helmersson U 2016 *Plasma Sources Sci. Technol.* **25** 065024
[15] Huo C, Lundin D, Raadu M A, Anders A, Gudmundsson J T and Brenning N 2013 *Plasma Sources Sci. Technol.* **22** 045005
[16] Huo C, Lundin D, Gudmundsson J T, Raadu M A, Bradley J W and Brenning N 2017 *J. Phys. D: Appl. Phys.* **50** 354003
[17] Mishra A, Kelly P J and Bradley J W 2010 *Plasma Sources Sci. Technol.* **19** 045014
[18] Rudolph M, Brenning N, Raadu M A, Hajihoseini H, Gudmundsson J T, Anders A and Lundin D 2020 *Plasma Sources Sci. Technol.* **29** 05LT01
[19] Rudolph M, Revel A, Lundin D, Hajihoseini H, Brenning N, Raadu M A, Anders A, Minea T M and Gudmundsson J T 2021 *Plasma Sources Sci. Technol.* **30** 045011
[20] Butler A, Brenning N, Raadu M A, Gudmundsson J T, Minea T and Lundin D 2018 *Plasma Sources Sci. Technol.* **27** 105005
[21] Window B and Savvides N 1986 *J. Vac. Sci. Technol.* A **4** 196
[22] Bohlmark J, Helmersson U, VanZeeland M, Axnäs I, Alami J and Brenning N 2004 *Plasma Sources Sci. Technol.* **13** 654
[23] Minea T, Kozák T, Costin C, Gudmundsson J T and Lundin D 2020 *High Power Impulse Mangetron Sputtering: Fundamentals, Technologies, Challenges and Applications* ed D Lundin, T Minea and J T Gudmundsson (Amsterdam: Elsevier) pp 159–221
[24] Raadu M A, Axnäs I, Gudmundsson J T, Huo C and Brenning N 2011 *Plasma Sources Sci. Technol.* **20** 065007
[25] Rudolph M, Hajihoseini H, Raadu M A, Gudmundsson J T, Brenning N, Minea T M, Anders A and Lundin D 2021 *J. Appl. Phys.* **129** 033303
[26] Hecimovic A and von Keudell A 2018 *J. Phys. D: Appl. Phys.* **51** 453001
[27] Held J, Maaß P A, Schulz-von der Gathen V and von Keudell A 2020 *Plasma Sources Sci. Technol.* **29** 025006
[28] Sheridan T E, Goeckner M J and Goree J 1990 *J. Vac. Sci. Technol.* A **8** 1623
[29] Čada M, Gudmundsson J T and Lundin D 2020 *High Power Impulse Magnetron Sputtering: Fundamentals, Technologies, Challenges and Applications* ed D Lundin, T Minea and J T Gudmundsson (Amsterdam: Elsevier) pp 81–110

[30] Brenning N, Merlino R L, Lundin D, Raadu M A and
     Helmersson U 2009 *Phys. Rev. Lett.* **103** 225003
[31] Boeuf J-P 2014 *Front. Phys.* **2** 74
[32] Alfvén H and Fälthammar C-G 1963 *Cosmical
     Electrodynamics* (*International Series of Monographs on
     Physics*) 2nd edn (London: Oxford University Press)

[33] Boström R 1964 *J. Geophys. Res.* **69** 4983
[34] Kozák T 2012 *Plasma Sources Sci. Technol.*
     21 025012
[35] Brenning N, Butler A, Hajihoseini H, Rudolph M, Raadu M A,
     Gudmundsson J T, Minea T and Lundin D 2020 *J. Vac. Sci.
     Technol.* A **38** 033008